Article

Lead-Free Perovskite Homojunction-Based HTM-Free Perovskite Solar Cells: Theoretical and Experimental Viewpoints

Sajid Sajid [1,2], Salem Alzahmi [1,2,*], Imen Ben Salem [3], Jongee Park [4] and Ihab M. Obaidat [2,5,*]

[1] Department of Chemical & Petroleum Engineering, United Arab Emirates University, Al Ain P.O. Box 15551, United Arab Emirates; s.bakhtawar@uaeu.ac.ae
[2] National Water and Energy Center, United Arab Emirates University, Al Ain P.O. Box 15551, United Arab Emirates
[3] College of Natural and Health Sciences, Zayed University, Abu Dhabi P.O. Box 144534, United Arab Emirates; imen.bensalem@zu.ac.ae
[4] Department of Metallurgical and Materials Engineering, Atilim University, Ankara 06836, Turkey; jongee.park@atilim.edu.tr
[5] Department of Physics, United Arab Emirates University, Al Ain P.O. Box 15551, United Arab Emirates
[*] Correspondence: s.alzahmi@uaeu.ac.ae (S.A.); iobaidat@uaeu.ac.ae (I.M.O.)

Abstract: Simplifying the design of lead-free perovskite solar cells (PSCs) has drawn a lot of interest due to their low manufacturing cost and relative non-toxic nature. Focus has been placed mostly on reducing the toxic lead element and eliminating the requirement for expensive hole transport materials (HTMs). However, in terms of power conversion efficiency (PCE), the PSCs using all charge transport materials surpass the environmentally beneficial HTM-free PSCs. The low PCEs of the lead-free HTM-free PSCs could be linked to poorer hole transport and extraction as well as lower light harvesting. In this context, a lead-free perovskite homojunction-based HTM-free PSC was investigated, and the performance was then assessed using a Solar Cell Capacitance Simulator (SCAPS). A two-step method was employed to fabricate lead-free perovskite homojunction-based HTM-free PSCs in order to validate the simulation results. The simulation results show that high hole mobility and a narrow band gap of cesium tin iodide ($CsSnI_3$) boosted the hole collection and absorption spectrum, respectively. Additionally, the homojunction's built-in electric field, which was identified using SCAPS simulations, promoted the directed transport of the photo-induced charges, lowering carrier recombination losses. Homojunction-based HTM-free PSCs having a $CsSnI_3$ layer with a thickness of 100 nm, defect density of 10^{15} cm^{-3}, and interface defect density of 10^{18} cm^{-3} were found to be capable of delivering high PCEs under a working temperature of 300 K. When compared to formamidinium tin iodide ($FASnI_3$)-based devices, the open-circuit voltage (V_{oc}), short-circuit density (J_{sc}), fill factor (FF), and PCE of $FASnI_3/CsSnI_3$ homojunction-based HTM-free PSCs were all improved from 0.66 to 0.78 V, 26.07 to 27.65 mA cm^{-2}, 76.37 to 79.74%, and 14.62 to 19.03%, respectively. In comparison to a $FASnI_3$-based device (PCE = 8.94%), an experimentally fabricated device using homojunction of $FASnI_3/CsSnI_3$ performs better with V_{oc} of 0.84 V, J_{sc} of 22.06 mA cm^{-2}, FF of 63.50%, and PCE of 11.77%. Moreover, $FASnI_3/CsSnI_3$-based PSC is more stable over time than its $FASnI_3$-based counterpart, preserving 89% of its initial PCE. These findings provide promising guidelines for developing highly efficient and environmentally friendly HTM-free PSCs based on perovskite homojunction.

Keywords: lead-free; HTM-free PSC; high efficiency; simulation; experiment

1. Introduction

Perovskite solar cells (PSCs) have attracted a lot of attention in the photovoltaic community in recent years owing to their high power conversion efficiencies (PCEs) and low-cost

fabrication [1,2]. Additionally, they have shown astounding improvements in photoelectric performance, which are a result of the superior optoelectronic characteristics of organic–inorganic halide perovskites, including their exceptionally high absorption coefficient, suitable band gap, ambipolar carrier transport property, and high defect tolerance. The PCEs of PSCs have lately approached 25.7% [3], which is a significant improvement. The commercialization of the PSCs is, however, limited by the use of costly organic hole trans-porting materials (HTMs) [4–8] and the toxicity of the lead (Pb) element [9]. The HTM-free PSCs are thought to significantly reduce the fabrication cost in this scenario. Consequently, a great deal of innovative studies focused on the HTM-free PSCs due to their inexpensive production costs and straightforward processing methods. The first methylammonium lead iodide and titanium oxide ($MAPbI_3/TiO_2$) heterojunction-based HTM-free PSCs showed PCEs as high as 7.28% [10]. Mei et al. reported PSCs with a heterojunction based on 5-ammoniumvaleric acid/methylammonium lead iodide/zirconium oxide/titanium ox-ide [$(5\text{-}AVA)_x(MA)_{1-x}PbI_3/ZrO_2/TiO_2$)], which yielded a certified PCE of 12.8% [11]. A PCE of 14.38% in $MAPbI_3$ heterojunction-based HTM-free PSCs was obtained through further investigation [12]. Huang developed HTM-free PSCs using 2,3,5,6-tetrafluoro-7,7,8,8-tetracyanoquinodimethane (F4TCNQ)-doped $MAPbI_3$ and demonstrated a PCE of 18.85% [13]. Kong et al. further reported one efficient method to increase the PCE of heterojunction-based HTM-free PSCs, and the PCE reached 19.42% [14]. Difluoroben-zylamine has recently been shown to function as an interfacial modifier to stabilize and improve the efficiency of HTM-free PSCs. Density-functional theory calculations and experiments showed that the fluorine atoms in the benzene ring can passivate defects at the surface or interface of the perovskites, enhancing the transfer of charge-carriers. As a result, PCE of the HTM-free PSC reached 14.6%, and after 1680 h of storage at 20–30% air humidity, the PCE of the unencapsulated device was still 92% of the initial PCE [15]. However, the reported PCEs of HTM-free PSCs hardly even reach 20%. In addition, these HTM-free PSCs contain toxic Pb, which limits their commercialization.

Tin (Sn)-based perovskites have garnered increased attention in the photovoltaics field due to their environmental friendliness compared to Pb-based PSCs [16]. Sn is the first and most likely alternative in the quest to replace lead in PSCs because, in comparison to Pb, it is less hazardous under various test conditions [17]. Sn-based perovskites have the potential to outperform their lead-based counterparts from a physical and theoretical perspective due to their lower bandgap, which is closer to the ideal values established by the Shockley–Queisser limit [18], high carrier mobility, and low exciton binding energy. Lee et al. reported that $FASnI_3$-based PSCs had a 4.8% PCE and good repeatability [19]. Later, Liao et al. showed an inverted PSC with a PCE of 6.22% [20]. The PCEs were further improved with pure $FASnI_3$ perovskite, up to 7 to 8% [21–24]. Higher PCEs might be at-tained by partially substituting other organic cations for formamidinium (FA). For instance, 8 to 9% PCEs have been obtained for enhanced film morphology and decreased carrier recombination by substituting 25% of the FA with methylammonium [25,26]. Over 9% PCE was achieved when bulky organic cations, such as phenylethylammonium, were added to the $FASnI_3$ perovskite lattice to generate a two-dimensional/three-dimensional hybrid perovskite film [27,28]. For Sn-based PSCs, a PCE of 9.6% was achieved by combining mixed guanidium and FA cations with the addition of ethylenediammonium diiodide [29]. More recently, after being post-treated with edamine Lewis base, a 10.18% PCE with $FA_{0.98}EDA_{0.01}SnI_3$ perovskite film has been reported [30]. Ning et al. [31] have recently created tin iodide/dimethyl sulfoxide ($SnI_2.(DMSO)_x$) complexes with improved coordi-nation using phenethylamine bromide (PEABr) as an additive by utilizing the interaction between I_2 and DMSO. In contrast, it was discovered that SnI_2 may be evenly distributed into the precursor solution and lessens the quantity of uncoordinated SnI_2. Obtaining more uniform perovskite films while guiding out-of-plane crystal orientation is possible with highly coordinated $SnI_2.(DMSO)_x$. The electron diffusion length in Sn-based film increased to roughly 80 nm and the PCE of 14.6% was obtained in PSCs as compared to reference films. Studies using SCAPS simulations have also shown that $FASnI_3$-based PSCs

can outperform lead-based ones [32]. Though great progress has been made in $FASnI_3$- or $MASnI_3$-based devices, the presence of organic ions in $FASnI_3$ poses some concerns about the durability of PSCs based on organic–inorganic hybrid Sn-based perovskites due to the volatile nature of organic constituents. Despite the poor morphology of their films, all-inorganic Sn-based perovskite may possibly be a better choice in this scenario. Since $CsSnX_3$ (here X represent halides: I, Br, or Cl) perovskites have tolerance factors that are closer to 1, the geometric arrangement of $CsSnX_3$ is more durable [33]. The $CsSnX_3$ perovskites have low energies for the phase transition from the orthorhombic to the tetragonal phase and, as a result, low phase transition temperatures [34]. Furthermore, the narrow band gap (1.3 eV), high absorption coefficient (10^4 cm^{-1}), and high hole mobility (42 cm^2 V^{-1} s^{-1}) of $CsSnI_3$ make it an excellent perovskite for high optical absorption and charge-carrier transport [35–38]. In comparison to the theoretical limit, the PCE of reported PSCs based on $CsSnI_3$ is only about 5.03% [39]. However, it is important to consider the oxidation of Sn^{2+} to Sn^{4+} because this will induce perovskite instability and decrease the efficiency of Sn-based PSCs [40]. In this context, metallic Sn was used by Lin et al. to reduce the Sn^{2+} from oxidation [41]. Other ways have been described, such as adding chemicals to the perovskite precursor, graphene–Sn quantum dots [42], tin halide (SnF_2/$SnCl_2$) [43–45], hypophosphorous [46], hydrazine [47], ethylenediammonium [48], and 1,4-bis(trimethylsilyl)-2 [49]. Therefore, such approaches might increase the Sn-based PSCs' stability, which would then increase their performance. However, the HTM-free PSCs seldom ever use the environmentally favorable homojunction-based perovskites. The perovskite and electron/hole transport materials form a heterojunction, but because of its excellent self-doping ability [50–53], the perovskite can also form a homojunction, which would lessen the presence of impurities that could act as carrier recombination centers [54]. The guided transport of the photo-induced electrons and holes may be aided by an internal electric field that arises in the perovskite homojunction, which would reduce additional charge-carrier recombination in the perovskite layer [55]. It is therefore a promising route to further improve PSC performances. If homojunction Sn-based perovskites might be theoretically and experimentally used to guide the fabrication of efficient HTM-free PSCs, it is currently unclear and scarcely reported.

As $FASnI_3$ and $CsSnI_3$ have similar perovskite crystal structures, fabricating $CsSnI_3$ on $FASnI_3$ may produce a homojunction layer that is high quality and has fewer defects. In light of this, conducting thorough theoretical and experimental examinations of the performance of $FASnI_3$/$CsSnI_3$ homojunction-based HTM-free PSCs could be a promising strategy to offer guidelines for environmentally friendly devices. In this regard, using SCAPS software, we first investigated the parameters of p-type $CsSnI_3$ that influence the performance of lead-free homojunction-based HTM-free PSCs. The HTM-free PSCs in this study use a lead-free homojunction-based perovskite ($FASnI_3$/$CsSnI_3$) as the photon harvesting layer. In the light absorption spectrum, the homojunction-based $FASnI_3$/$CsSnI_3$ perovskite demonstrated better photon harvesting. Additionally, the homojunction's built-in electric field, which was identified using SCAPS simulations, promotes the directed movement of the photo-induced charges, lowering carrier recombination losses. With optimal conditions, the lead-free homojunction-based HTM-free PSCs display a PCE of 19.02%. Moreover, a homojunction-based HTM-free PSC was fabricated to verify the validity of the simulations. According to the experimental approach, the $FASnI_3$/$CsSnI_3$ perovskite-based homojunction was fabricated by a two-step process [55]. As a result, the $FASnI_3$/$CsSnI_3$ homojunction-based HTM-free device demonstrated better performance with a PCE of 11.77% compared to the $FASnI_3$-based HTM-free PSC (PCE = 8.94%).

2. Materials and Methods

2.1. Simulation Procedure

For experimental scholars investigating solar cells, finding the ideal structure and materials have always been a major difficulty. This procedure can be expedited by the simulation tool. The unique capabilities of the SCAPS include, but are not restricted to, modeling up to seven layers and computing numerous parameters, such as spectral response, energy bands, J-V curve, and defect density, by only resolving three fundamental semiconductor equations. It is simple to operate and can be utilized in both light and dark conditions. Key processes in photovoltaic systems are defined by SCAPS modeling techniques, allowing for the intuitive and systematic classification of optimal operating conditions for each parameter. In this research, a lead-free homojunction-based perovskite with a device layout of $FTO/TiO_2/FASnI_3/CsSnI_3/Au$ was proposed in HTM-free PSCs, as illustrated in Figure 1a,b. The illumination source in the simulation was the AM l.5G solar radiation spectrum with an intensity of 1000 $W \cdot m^{-2}$. Important material parameters were gathered from prior experimental reports and are summarized in Table 1 to validate the viability of the simulations. Two interface layers were introduced: one between the $FASnI_3$ and $CsSnI_3$ and the other one between the $CsSnI_3$ and gold (Au) electrode, accounting for the interfacial defect density (denoted by IDL1 and IDL2 in Table 1). The defects in the perovskite layer were configured to have a characteristic energy of 0.1 eV and to be in a neutral Gaussian distribution with energy 0.6 eV above the valence band. Interfacial defects were regarded as neutral single defects with distribution energy of 0.6 eV above the valence band.
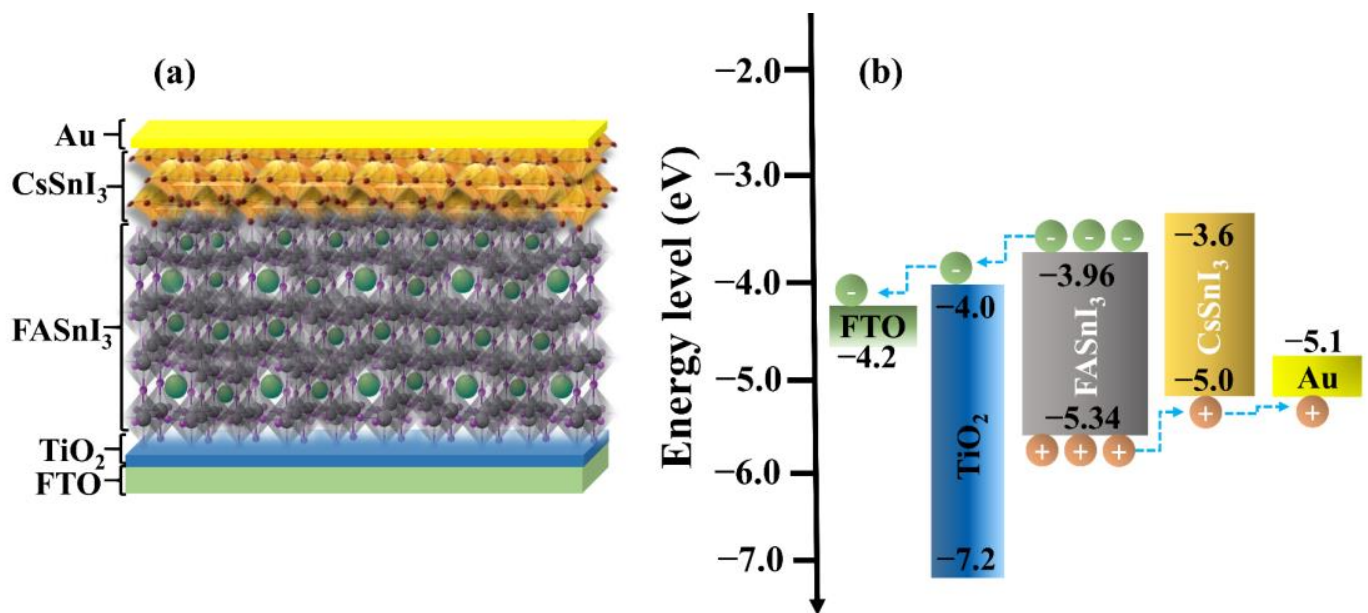

Figure 1. Schematic illustrations of a homojunction-based HTM-free PSC (**a**) and a corresponding energy band diagram of each material used in the simulation (**b**).

Table 1. Material parameters for the homojunction-based HTM-free PSC. Here L, Φ, ε_r, E_g, X, N_c, N_v, μ_n, μ_p, N_A, N_D, and N_t represent thickness, work-function, relative permittivity, energy band gap, electron affinity, effective conduction band density, effective valance band density, electron mobility, hole mobility, acceptor doping density, donor doping density, and defect density, respectively.

Parameters	FTO [56,57]	TiO$_2$ [55,58,59]	FASnI$_3$ [60–62]	IDL1 [63]	CsSnI$_3$ [35–38]	IDL2 [64,65]	Au [66,67]
L (nm)	500	150	400	15	100	15	80
Φ (eV)	4.2	4.1	—	—	—	—	5.1
ε_r	9	10	25	10	25	10	—
E_g (eV)	3.4	3.2	1.4	1.5	1.3	1.5	—
X (eV)	4	4	3.93	3.93	3.7	3.93	—
N_c (cm^{-3})	2.3×10^{18}	1.2×10^{19}	2.5×10^{19}	2.5×10^{19}	1.4×10^{19}	2.5×10^{19}	—
N_v (cm^{-3})	2.3×10^{19}	1.2×10^{20}	1.8×10^{20}	2.5×10^{20}	1.4×10^{18}	2.5×10^{20}	—
μ_n (cm^{-2} V^{-1} s^{-1})	0.3	0.006	0.6	0.6	0.6	0.6	—
μ_p (cm^{-2} V^{-1} s^{-1})	0.1	0.005	0.6	0.6	42	0.6	—
N_A (cm^{-3})	0	0	1×10^{18}	1×10^{18}	1×10^{17}	1×10^{18}	—
N_D (cm^{-3})	2×10^{19}	5×10^{19}	1×10^{18}	1×10^{18}	0	1×10^{18}	—
N_t (cm^{-3})	1×10^{16}	1×10^{17}	1×10^{16}	1×10^{18}	1×10^{15}	1×10^{18}	—

Using SCAPS-1D software developed by researchers at the University of Ghent, the photovoltaic performance of the devices under AM1.5G solar illumination was examined [68]. By resolving the following Equations (1)–(3), which are encoded in SCAPS-1D, it was possible to obtain the current-voltage (J-V) characteristic curves, external quantum efficiency (EQE), generation/recombination of charges, and electric field distribution.

$$\frac{d}{dx}\left(-\varepsilon(x)\frac{d\Psi}{dx}\right) = q\left[p(x) - n(x) + N_d^+(x) - N_a^-(x) + P_t(x) - n_t(x)\right] \tag{1}$$

$$\frac{dP_n}{dt} = G_p - \frac{P_n - P_{n0}}{\tau_p} - P_n\mu_n\frac{dE}{dx} - \mu_p E\frac{dP_n}{dx} + D_p\frac{d^2P_n}{dx^2} \tag{2}$$

$$\frac{dn_p}{dt} = G_n - \frac{n_p - n_{p0}}{\tau_n} - n_p\mu_p\frac{dE}{dx} - \mu_n E\frac{dn_p}{dx} + D_n\frac{d^2n_p}{dx^2} \tag{3}$$

where ε, Ψ, q, n, p, n_t, p_t, N_d, N_a, G, D, and E represent the permittivity, electrostatic potential, elementary charge, density of free electrons, density of free holes, density of trapped electrons, density of trapped holes, donor doping density, acceptor doping density, generation rate, diffusion coefficient, and electric field, respectively.

2.2. Experimental Procedure
2.2.1. Fabrication of PSCs

The FTO-substrates were ultrasonically cleaned after being immersed for 20 min in acetone, deionized water, detergent solution, and isopropyl alcohol, respectively. The FTO-substrates were treated with UV-ozone for 15 min following nitrogen blow drying. An aqueous stock solution of 2 M TiCl$_4$ (stored in the freezer) was diluted to the desired proportion after cleaning the FTO-substrates. The as-cleaned substrates were then dipped in this solution and maintained in a closed vessel in a 70 °C oven for one hour. To create a compact layer of TiO$_2$ (denoted as c-TiO$_2$), the substrates were dried at 100 °C in the air for an hour after being rinsed with deionized water and ethanol. Spin-coating the TiO$_2$ nanoparticles paste in ethanol at 2000 rpm for 25 s resulted in the deposition of a mesoscopic TiO$_2$ layer (denoted as m-TiO$_2$). The substrate was subsequently annealed for 20 min at 500 °C. After annealing, a diluted TiCl$_4$ aqueous solution in deionized water was applied to the FTO/c-TiO$_2$/m-TiO$_2$ substrate for 20 min at 70 °C. The substrate was

then exposed to UV-ozone for 10 min. SnI_2 (0.143 g) and FAI (0.140 g) were combined with 1 mL of DMSO to form the precursor solution for the $FASnI_3$. The $FASnI_3$ layer was then created by one-step spin-coating of the $FASnI_3$ precursor solution for 25 s at 4000 rpm. Then, 0.5 mL of diethyl ether was carefully injected during the spinning process as an anti-solvent to speed up the formation of perovskite film. The resultant perovskite layers were annealed for 10 s at 60 °C and then for 12 min at 100 °C. Then, the $FTO/c-TiO_2/m$-$TiO_2/FASnI_3$ coated substrates were used to fabricate a homojunction $FASnI_3/CsSnI_3$-based perovskite layer, as schematically illustrated in Figure 2. With a SnI_2 thickness of $\sim$65 nm (formed by vapor deposition) and a dipping duration of 50 s (equivalent to a SnI_2/CsI ratio of 1.6), the top $CsSnI_3$ perovskite layer was produced. The as-prepared $FTO/TiO_2/FASnI_3/CsSnI_3$ substrate was then annealed at 70 °C for 10 min. Note that we followed the two-step method from a previous report [55]. Lastly, to fabricate 80 nm electrodes onto the perovskite films and complete the $FTO/c-TiO_2/m-TiO_2/FASnI_3/Au$ and $FTO/c-TiO_2/m-TiO_2/FASnI_3/CsSnI_3/Au$ devices, gold was thermally evaporated.
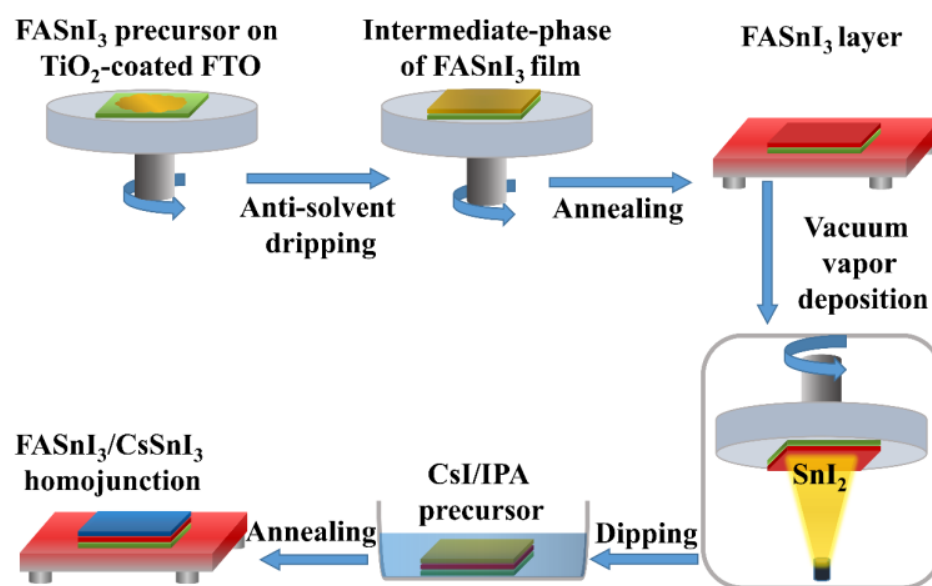

Figure 2. The illustration for the fabrication of the $FASnI_3/CsSnI_3$ homojunction-based layer.

2.2.2. Characterization of Thin-Films and PSCs

The surface and cross-sectional morphologies were examined using a scanning electron microscope (Hitachi S-4800). The absorption spectrum was determined using a UV–Vis spectrophotometer (UV-2600). Using Edinburg PLS 980, the steady-state PL spectra of the obtained samples were examined. The TRPL decay of the perovskite layers was shown using a transient state spectrophotometer (Edinburgh Institute F900) and a 485 nm laser. For the J-V characteristic curves, the devices were measured using a source meter (Keithley 2400) using forward (-0.1 to 1.2 V) or reverse (1.2 to -0.1 V) scans from a solar simulator (XES-301S+EL-100) under AM 1.5G illumination with a power intensity of 1000 W cm^{-2}. The step voltage was set to 12 mV, and the delay duration was 10 ms. The QE-R system (Enli Tech.) was used to determine the EQEs of the as-prepared devices.

3. Results and Discussion

We first explore significant parameters (such as thickness, doping density, and interface defect density at IDL1 and IDL2, and defect density of the $CsSnI_3$) that affect the performance of the homojunction-based HTM-free PSCs in order to acquire optimum values and provide guidelines for the experimental approaches. These parameters were left the same for the remaining layers of the as-simulated HTM-free PSCs. The performance variances in the cells as a function of the aforementioned parameters are elaborated in the following discussion.

Given that the thickness of the CsSnI$_3$ has a significant role in the incident light absorption and charge-carrier generation, the PSC's performance will be affected by varying this thickness. The perovskite layer in a PSC must be thick enough to maximize light absorption yet thick enough to boost the collection of photo-generated charge-carriers. The collection efficiency is determined by the competition between recombination and charge transfer to the corresponding contacts. Therefore, choosing the right CsSnI$_3$ thickness will be crucial for developing efficient homojunction-based HTM-free PSCs. Figure 3 illustrates how the photovoltaic performance and energy levels of the as-simulated HTM-free PSCs vary with CsSnI$_3$ thickness. As noted in Figure 3a, the J$_{sc}$ was increased significantly from 27.08 to 30.09 mA cm^{-2}, which could be attributed to a higher generation of charge-carriers due to an improved capability of the homojunction-based perovskite layer for light harvesting. According to the simulated quantum efficiency, as shown in Figure 3b, the absorption spectrum broadens with increasing CsSnI$_3$ thickness. It should be noted that the J$_{sc}$ grows slowly and tends to saturate when the CsSnI$_3$ thickness exceeds 300 nm because too thick perovskite could result in a significant charge-carrier recombination [64]. Figure 3c shows how the perovskite layer tends to saturate the PCE at larger thicknesses. This is because thick layers make it hard for charge-carriers to be collected in a timely manner, and they recombine before they reach the relevant electrodes. Even though the simulation results showed that PSCs with thicker CsSnI$_3$ layers (more than 100 nm and less than 400 nm) performed better, we still believed that it would be difficult to fabricate CsSnI$_3$ layers on FASnI$_3$ that were thicker than 100 nm because it is known that the precursor solvent used to make CsSnI$_3$ will dissolve the FASnI$_3$ bottom layer. Figure 3d shows the energy levels of the HTM-free PSCs as a function of CsSnI$_3$ thickness, demonstrating that the built-in electric potential (V_{bi}) is weakly influenced by the thickness of CsSnI$_3$. This is because the doping density, as shown by Equation (4), is the primary factor controlling the V_{bi} [69,70].

$$V_{bi} = \frac{kT}{q} ln \frac{N_A N_D}{n_i^2} \tag{4}$$

where k, T, q, N_A, N_D, and n_i represent Boltzmann constant, temperature, elementary charge, acceptor doping density, donor doping density, and intrinsic density, respectively. These findings reveal that when the light-harvesting perovskite layer is very thin, poor photon absorption results in low photocurrents; however, if the perovskite layer is very thick, recombination issues develop due to poor charge-carrier extraction efficiency. The simulation findings showed that a CsSnI$_3$ layer with an optimal thickness of 100 nm can be used to obtain efficient homojunction-based HTM-free PSCs.

Another crucial element that influences the PSC's photovoltaic metrics is the doping density of the perovskite layer. We therefore look at the critical role that the CsSnI$_3$ doping density plays in the homojunction-based HTM-free PSCs. Figure S1 shows the alterations in the J-V characteristic curves, PCEs, and energy levels with changes in the acceptor doping density (N_A). Figure S1a,b shows that no discernible changes in the photovoltaic parameters were seen at N_A from 10^{13} to 10^{15} cm^{-3}, demonstrating that the relatively modest doping density does not alter the inherent property of CsSnI$_3$. The better photovoltaic performance of the as-simulated HTM-free PSCs can be due to the larger V_{bi} (as shown in Figure S1c,d and Equation (4)) brought on by the larger N_A, which is increased from 10^{15} to 10^{18} cm^{-3}. As shown in Figure S1b, the PCE improves when the N_A increases from 10^{15} to 10^{18} cm^{-3} and it begins to decline as the N_A of the CsSnI$_3$ exceeds 10^{18} cm^{-3}. High doping density can help with charge-carrier separation, but too much doping inhibits charge-carrier mobility and causes substantial charge-carrier recombination, which lowers PCE. The simulation results reveal that the optimal value of N_A is close to 10^{18} cm^{-3}.
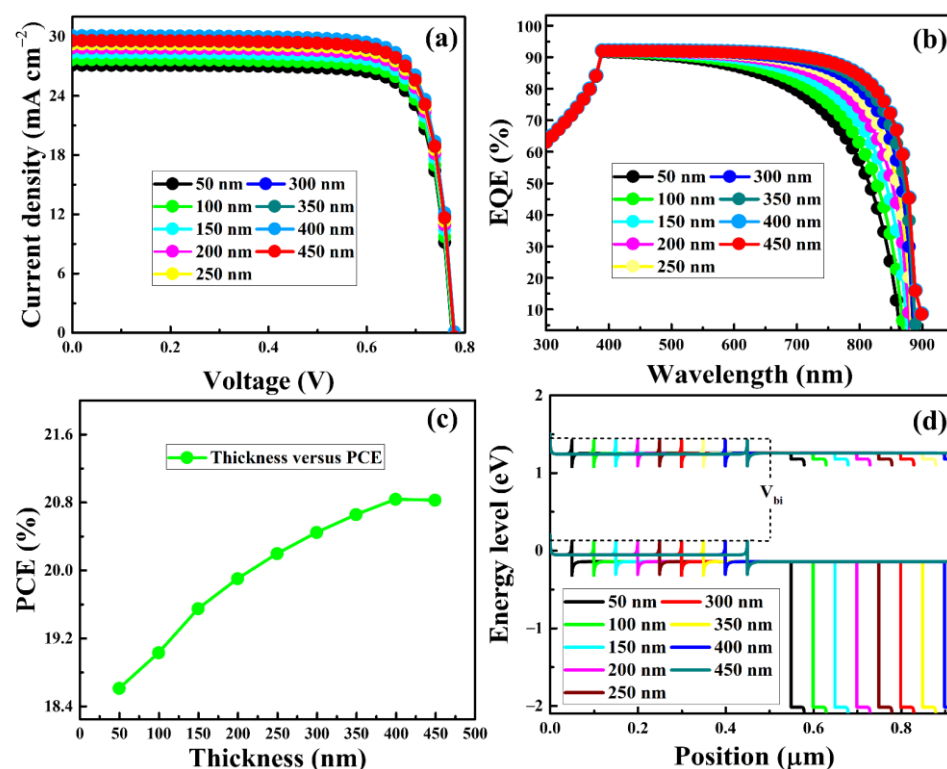
Figure 3. Performance of the homojunction-based HTM-free PSCs as a function of perovskite (CsSnI$_3$) layer thickness. The current-voltage (J-V) characteristic curves (**a**), external quantum efficiencies (EQEs) (**b**), power conversion efficiencies (PCEs) (**c**), and energy levels (**d**).

The perovskite layer is the main part for the generation of charge-carriers. As a result, the PSC's performance is greatly influenced by the properties of the perovskite layer. Defect density is a crucial indicator of how well the perovskite layer performs. Therefore, fabricating high-quality perovskite active layers with low defect densities and less nonradiative recombination is essential for producing highly efficient PSCs. The nature and density of defect states in perovskites are very sensitive to the film deposition conditions, according to prior calculations and experimental data [71]. Due to the lack of stoichiometric compositions at the surfaces of grains and the possibility that perovskite constituents could disintegrate during the thermal annealing process and leave defects, it is believed that the majority of the defects in perovskite films are found at the grain boundaries or the interface [54,72]. In this context, we have investigated the impact of defect densities on the performance of the homojunction-based HTM-free PSCs, specifically the effect of bulk defects in the perovskite layer and defects at the interfaces. Figure 4a displays the J-V characteristic curves as function of defect density in the CsSnI$_3$. It demonstrates that the PCE begins to decline when the perovskite layer has a high defect density. Higher defect densities in low-quality perovskite layers raise carrier recombination rates because defects trap charge-carriers, as seen in Figure 4b. It is currently challenging to significantly reduce the defect density in the CsSnI$_3$ layer due to the fact that the CsSnI$_3$ perovskite is unstable in the air and requires sophisticated fabrication techniques [36,45,73]. According to the simulation results, high device performance can be obtained with defect density from 10^{15} to 10^{16} cm^{-3} in the CsSnI$_3$ layer.
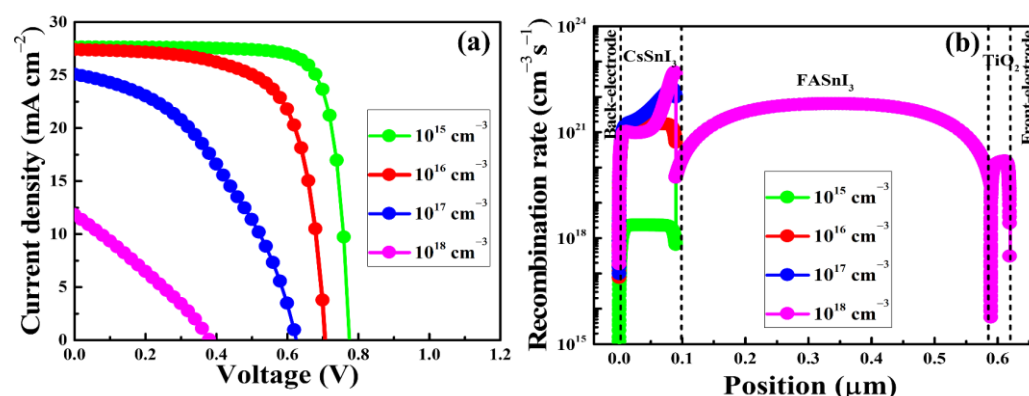
Figure 4. The current-voltage (J-V) characteristic curves (**a**) and charge-carrier recombination rate (**b**) of the as simulated homojunction-based HTM-free PSCs as a function of defect density of $CsSnI_3$.

In addition, the performance of PSCs is significantly influenced by the characteristics of the interface layers. It is widely speculated that low-quality interfaces result in larger surface/interface defect densities, which in turn increase the recombination of charge-carriers [74]. We assume that the defect densities of IDL1 and IDL2 range between 10^{18} and 10^{22} cm^{-3} in order to discuss the impact of the defect density of the interface layers on the PSC performance. The J-V characteristic curves and PCEs of the as-simulated homojunction-based HTM-free PSCs as a function of defect densities in IDL1 and IDL2 are shown in Figure S2a–d. These graphs demonstrate that lowering defect density in the interface layer will boost the PCE. Evidently, the effect of the defect density on the J-V characteristics becomes noticeable when the defect density is more than 10^{18} cm^{-3}, which deteriorates the performance of the homojunction-based HTM-free PSCs. It is clear that IDL1 has a higher impact on PCE than IDL2, which can be explained by the possibility that defects may occur during the deposition of the $CsSnI_3$ layer on $FASnI_3$ thin-film. Based on simulation results, the defect densities of IDL1 and IDL2 should be less than 10^{19} cm^{-3}, in order to attain the desired efficiency of homojunction-based HTM-free PSCs.

The homojunction-based $FASnI_3/CsSnI_3$ is utilized in this study as an absorber layer in the lead-free HTM-free PSCs. It is revealed that the thickness, doping density, and defect density of the $CsSnI_3$ layer should be around 100 nm, 10^{17} cm^{-3}, and 10^{16} cm^{-3}, respectively, for the HTM-free PSCs to perform at their best. The optimal performance of the as-simulated HTM-free PSCs is shown in Figure 5 and the photovoltaic parameters are listed in Table 2. The improvement of the overall performance of the homojunction-based HTM-free PSC (Figure 5a) is attributed to the increased photo-generated charge-carrier generation rate (Figure 5b) and extended absorption of the homojunction-based $FASnI_3/CsSnI_3$ (Figure 5c). The electric field within the PSC might be impacted by unintentional defects in the bulk or at device interfaces. As shown in Figure 5d, the electric field generated by the $FASnI_3/CsSnI_3$ homojunction with a defect density of 10^{16} cm^{-3} and doping density of 10^{17} cm^{-3} enables directed charge-carrier transfer. Free holes will rise as electron concentrations decrease in the p-type perovskite region, exhibiting carrier-directed transport [55]. It should be noted that when the doping density is equal to or lower than the defect density, the perovskite layers become semi-insulating and fail to form the desired p-n homojunction [75]. Based on the simulation results, the PCE of $FASnI_3/CsSnI_3$ homojunction-based HTM-free PSCs significantly increased from 14.62 to 19.03% when compared to the devices based on a bare $FASnI_3$ perovskite layer.
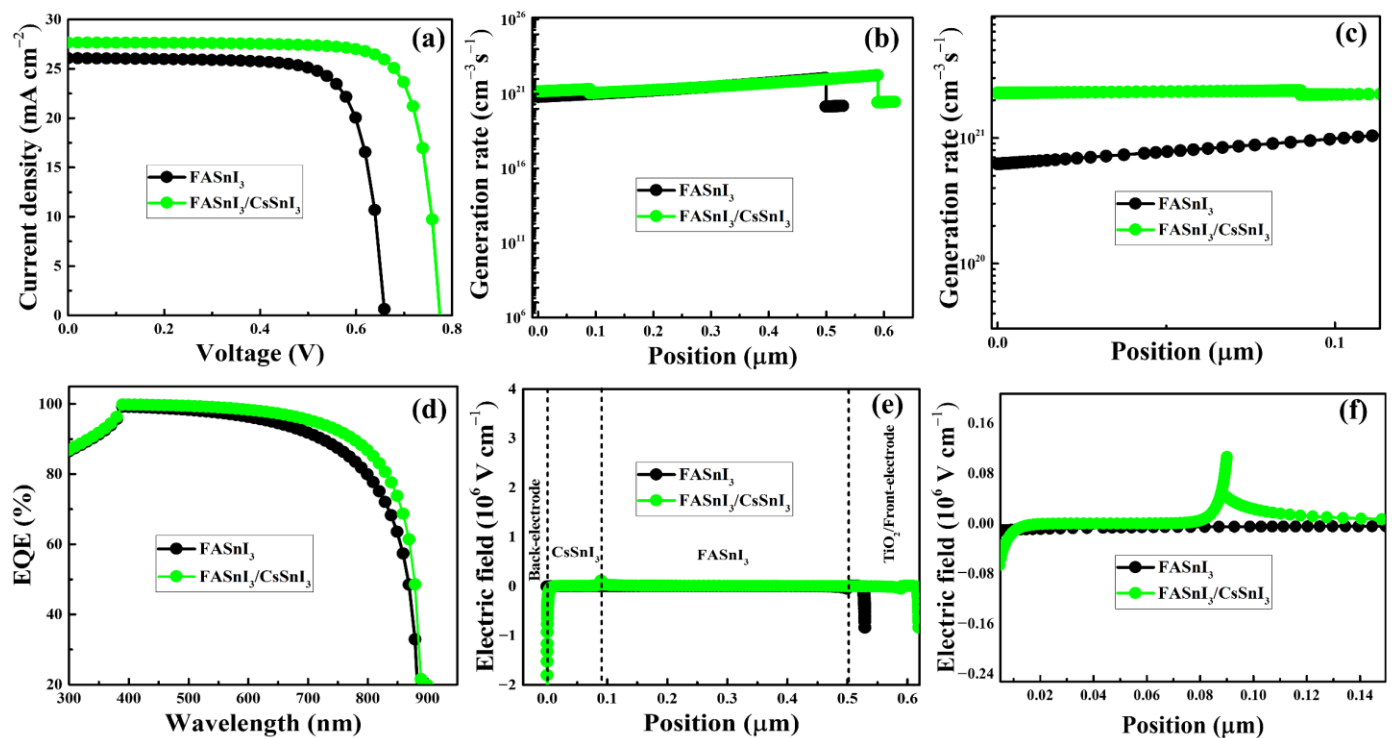
Figure 5. Photovoltaic performance of the HTM-free PSCs utilizing bare FASnI$_3$ and homojunction-FASnI$_3$/CsSnI$_3$ perovskite. The J-V characteristic curves (**a**), charge-carrier generation rate (**b**), zoomed-in graph showing the improved charge-carrier generation (**c**), external quantum efficiencies (EQEs) (**d**), and electric field distribution (**e**), zoomed-in graph, indicating enhanced electric field (**f**).

Table 2. Photovoltaic parameters of the as-simulated homojunction-based HTM-free PSCs under illumination of AM1.5G with an intensity of 1000 W·m^{-2}.

Device Design	V_{oc} (V)	J_{sc} (mA cm^{-2})	FF (%)	PCE (%)
FTO/TiO$_2$/FASnI$_3$/Au	0.66	26.07	76.37	14.62
FTO/TiO$_2$/FASnI$_3$/CsSnI$_3$/Au	0.78	27.65	79.74	19.03

Meanwhile, the performance of the as-simulated HTM-free PSCs is tested as a function of operating temperature. For PSC simulation, 300 K is typically the testing temperature used. However, under experimental conditions, the operational temperature is typically higher than the simulation. Here, under the conditions stated in Table 1, the working temperature for the efficient homojunction-based HTM-free PSC was maintained at 300 K. It is important to note that high temperatures may cause devices to deform and undergo higher stress [76], which will increase interfacial defects and poor interconnectivity between the layers, lowering the photovoltaic parameters, as depicted in Figure S3. Despite the modeling findings demonstrating reduction in the photovoltaic parameters of the as-simulated HTM-free PSCs, the stability of the Sn-based PSCs can be increased, though, by modifying the active layer morphology [77,78], using a controlled environment for film formation [36,47], and adding tin halides (SnF$_2$ or SnCl$_2$) to the perovskite precursor solution [79]. According to some studies, FASnI$_3$ and CsSnI$_3$ exhibit significantly better thermal and photochemical stability with regard to both light and high temperatures [45,80,81].

The performance of the homojunction-based PSCs was assessed, and then FASnI$_3$ and FASnI$_3$/CsSnI$_3$ perovskite thin-films were experimentally fabricated. To make the FASnI$_3$ thin-film, a one-step spin-coating was taken. Contrarily, a two-step technique was used to fabricate the CsSnI$_3$ layer on top of a FASnI$_3$ layer (made through a one-step spin-coating process), as shown in Figure 2. Both perovskite (FASnI$_3$ and FASnI$_3$/CsSnI$_3$) layers are

compact and pinhole-free, as shown by surface morphologies and cross-sectional SEM images (Figure 6a–d), which will aid in charge-carrier transport and prevent shunting paths. Figure 6e shows the optical absorption of the $FASnI_3$ and $FASnI_3/CsSnI_3$ thin-films. According to the results, the $FASnI_3/CsSnI_3$ sample exhibits improved optical absorption, which is advantageous for the generation of photo-induced charge-carriers in the homojunction-based HTM-free PSCs. The charge-carrier dynamics within as-prepared samples were investigated by steady-state photoluminescence (PL) and time-resolved photoluminescence (TRPL) spectroscopies as depicted in Figure 6. Compared to $FASnI_3$, the PL of the $FASnI_3/CsSnI_3$ sample decreases, as shown in Figure 6f. The higher quenched PL spectra shows that in the final device, the $FASnI_3/CsSnI_3$ film has a substantially higher charge extraction and transfer efficiency. The $FASnI_3/CsSnI_3$ sample has a shorter decay lifespan than the $FASnI_3$ sample, according to the TRPL spectra (Figure 6g), indicating that the charge-carriers were extracted quickly at the $FASnI_3/CsSnI_3$ interface. In order to maximize the efficiency of charge-carrier transport within homojunction-based HTM-free PSCs, the $FASnI_3/CsSnI_3$ layer could reduce charge losses.
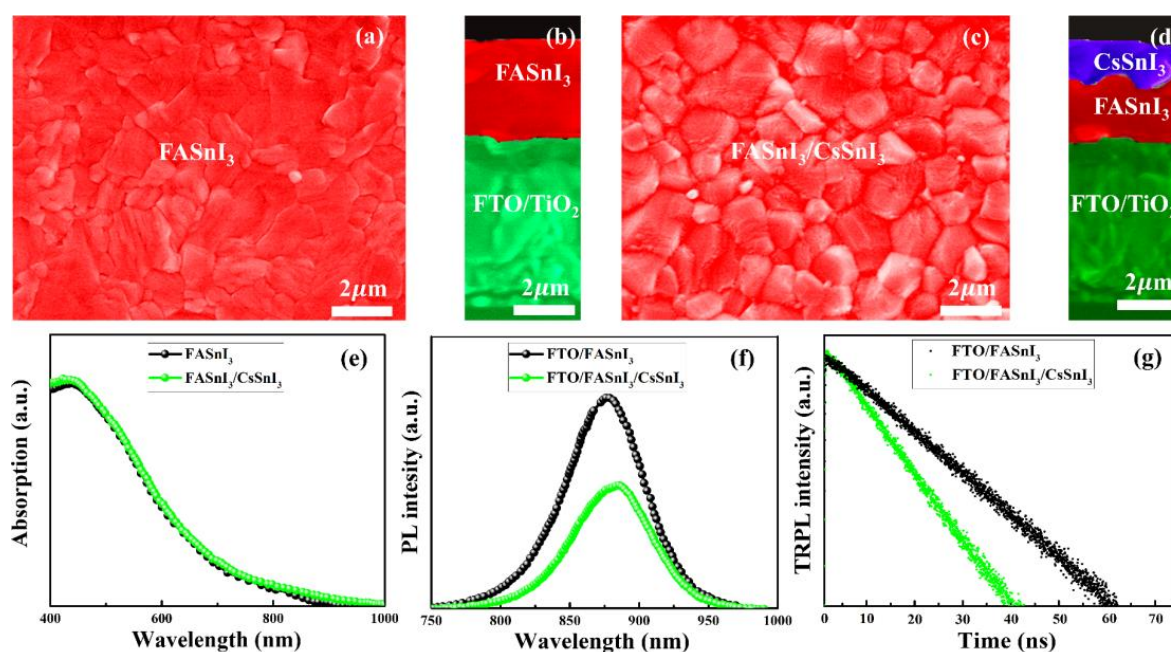

Figure 6. Surface and cross-sectional SEM images of $FASnI_3$ thin-films (**a**,**b**) and $FASnI_3/CsSnI_3$ thin-films (**c**,**d**). UV–Vis absorption spectra (**e**), PL spectra, and TRPL spectra of the as-prepared samples (**f**,**g**).

We fabricated two different types of PSCs (FTO/c-TiO_2/m-TiO_2/$FASnI_3$/Au and FTO/c-TiO_2/m-TiO_2/$FASnI_3$/$CsSnI_3$/Au) while taking into consideration the aforementioned simulation results and optoelectronic characteristics of the perovskite thin-films. Figure 7a,b shows the cross-sectional SEM images of the PSCs prepared using $FASnI_3$ and $FASnI_3/CsSnI_3$ layers. The surface and cross-sectional SEM results show that the functional layers in both PSCs were compact and free of pinholes. The photovoltaic parameters are presented in Table 3. Figure 7c displays the J-V characteristic curves for the $FASnI_3$ and $FASnI_3/CsSnI_3$ devices under AM1.5G illumination. The average PCE of the $FASnI_3/CsSnI_3$ HTM-free PSC was 11.77%, with a V_{oc} of 0.84 V, a J_{sc} of 22.06 mA cm^{-2}, and an FF of 63.50%. In comparison, the PCE of the $FASnI_3$ device was significantly lower with PCE of 8.94%, V_{oc} of 0.79 V, J_{sc} of 21.20 mA cm^{-2}, and FF of 53.35%. The efficient extraction of charge-carriers and improved light harvesting are attributable for the improved performance of $FASnI_3/CsSnI_3$-based PSCs, as depicted in Figure 7d. The simulation results showed higher PCEs than those for experimentally prepared HTM-free PSCs, which we believed might be due to the defects in the perovskite layer. In this scenario, it is possible to

further improve performance of the homojunction-based HTM-free PSCs by incorporating various additives into the perovskite precursor, such as N,N′-methylenebis(acrylamide) and pentafluorophen-oxyethylammonium iodide [82,83]. The diffusion of the Au metal, which may create serious deep centers, could be another possible cause of the inferior performance of the as-prepared HTM-free PSCs. In this context, we suggest interfacial engineering to promote favorable charge transport in perovskites [84]. Another potential method to increase the efficacy of the HTM-free PSCs is to introduce a plasmonic effect, which has been shown to promote the optoelectronic characteristics of the perovskites [85,86].
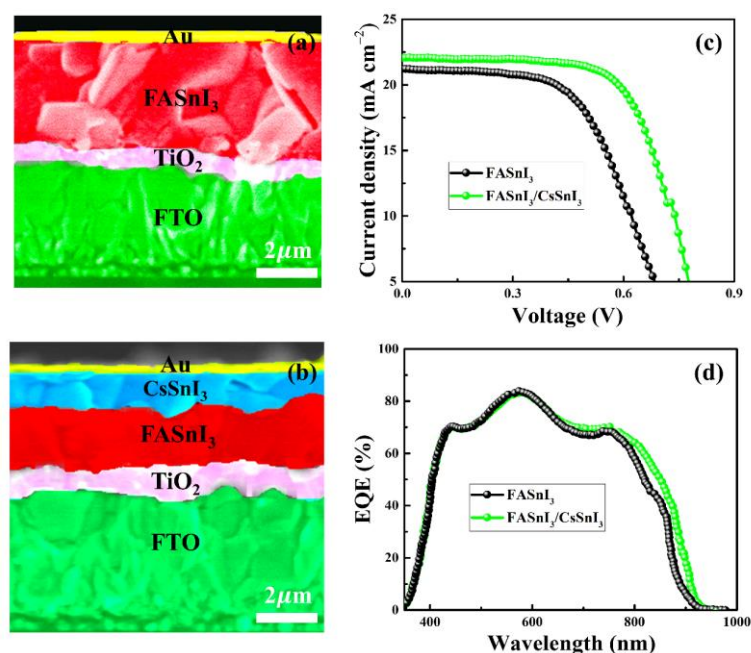

Figure 7. The cross-sectional SEM images (**a,b**), J-V characteristic curves (**c**), and EQEs of the HTM-free PSCs using $FASnI_3$ and $FASnI_3/CsSnI_3$ as photo-absorber layers (**d**).

Table 3. Photovoltaic parameters of the as-fabricated HTM-free PSCs under illumination of AM1.5G with an intensity of 1000 $W \cdot m^{-2}$.

Device Design	V_{oc} (V)	J_{sc} (mA cm^{-2})	FF (%)	PCE (%)
$FTO/TiO_2/FASnI_3/Au$	0.79	21.20	53.35	8.94
$FTO/TiO_2/FASnI_3/CsSnI_3/Au$	0.84	22.06	63.50	11.77

In addition, the statistical data of PSCs based on $FASnI_3$ and $FASnI_3/CsSnI_3$ (33 devices for each) were obtained, as shown in Figure S4a. The statistical data show that HTM-free PSCs prepared with the $FASnI_3/CsSnI_3$ homojunction have higher PCEs and better reproducibility than the $FASnI_3$-based HTM-free devices. The PCEs for $FASnI_3/CsSnI_3$ homojunction-based HTM-free PSCs fall within a narrow range, whereas $FASnI_3$-based devices exhibit PCEs that are widely distributed. The average PCE for the $FASnI_3$-based devices reached 5.78%. The average PCE for $FASnI_3/CsSnI_3$ homojunction-based HTM-free PSCs, in comparison, reaches up to 10.83%. The high PCE and reproducibility of the HTM-free PSCs are two important characteristics, but another is their stability. The steady-state J_{sc} and PCE of the $FASnI_3/CsSnI_3$-based HTM-free PSCs were initially tracked at a maximum power point at a bias voltage of 0.9 V at room temperature under AM 1.5G illumination, as shown in Figure S4b. After 140 s of continuous illumination, the $FASnI_3/CsSnI_3$-based HTM-free PSC exhibits a stabilized PCE of 11.58%, which is considerably near to the maximum PCE of 11.77% for the identical PSC. Further, unsealed PSCs made using $FASnI_3$ and $FASnI_3/CsSnI_3$ perovskites had their long-term stability tested every 45 min for 500 min

under AM 1.5G illumination, as depicted in Figure S4c. After each stability test, the measured devices were kept in a glass oven at 25 °C and 55% humidity. Figure S4c illustrates the superior stability of the $FASnI_3$/$CsSnI_3$-based HTM-free PSCs over $FASnI_3$-based devices. After 500 min of testing, the efficiency of $FASnI_3$/$CsSnI_3$-based HTM-free PSCs slightly decreases from 11.73 to 10.43% while maintaining 89% of the original PCE. The PCE of $FASnI_3$-based PSCs under the identical testing conditions declined sharply from 8.58 to 1.04%, demonstrating poor stability and quick degradation. The protection of the $CsSnI_3$ layer, which lessens the interaction of degradation factors such as moisture and oxygen present in the environment, can be attributed to the higher stability of $FASnI_3$/$CsSnI_3$-based devices.

4. Conclusions

In this research, numerical analysis was first used to determine the optimum conditions for fabricating highly efficient homojunction-based HTM-free PSCs. There were a number of factors that have all been carefully considered and the influences on the performance of the HTM-free PSCs were studied. The simulation results revealed the broad absorption spectrum by the inclusion of $CsSnI_3$, and the high hole mobility facilitated the charge-carrier transportation. For effective photon harvesting in highly efficient HTM-free PSCs, a $CsSnI_3$ layer thickness of approximately 100 nm was required. The optimal doping density for the $CsSnI_3$ layer was between 10^{15} and 10^{18} cm^{-3}. The simulation results also showed that the PSC operates better when its defect density was suitable, but that it performs poorly and has a greater charge-carrier recombination rate when it has too many defects. The simulation method indicated that the $FASnI_3$/$CsSnI_3$ homojunction-based HTM-free PSCs displayed PCEs up to 19.03% under optimal conditions. Taking into account the aforesaid simulation results, an experimental $FASnI_3$/$CsSnI_3$ homojunction-based HTM-free PSC with a configuration of FTO/c-TiO$_2$/m-TiO$_2$/$FASnI_3$/$CsSnI_3$/Au was fabricated. Compared to the $FASnI_3$/$CsSnI_3$-based HTM-free PSC, which delivered a PCE of 11.77%, the PCE of the $FASnI_3$ device was much lower (8.94%). The $FASnI_3$/$CsSnI_3$-based HTM-free PSC additionally showed long-term stability while retaining 89% of its initial efficiency. Our study is crucial for providing new viewpoints on using lead-free homojunction perovskites and for further enhancing the performance of lead-free homojunction-based HTM-free PSCs.

Supplementary Materials: The following supporting information can be downloaded at: https://www.mdpi.com/article/10.3390/nano13060983/s1, **Figure S1**: The current-voltage (J-V) characteristic curves (a), power conversion efficiencies (PCEs) (b), energy levels (c) and zoomed-in energy levels (d) of the as-simulated homojunction-based HTM-free PSCs as a function of doping density of $CsSnI_3$. Note that the $FASnI_3$/$CsSnI_3$ region is where the zoomed-in energy levels were taken; **Figure S2**: The current-voltage (J-V) characteristic curves and power conversion efficiencies (PCEs) of the as-simulated homojunction-based HTM-free PSCs as a function of defect density in IDL1 (a, b) and IDL2 (c, d); **Figure S3**: Photovoltaic performance of the as-simulated homojunction-based PSCs as a function of temperature; **Figure S4**: Statistics of the HTM-free PSCs with $FASnI_3$ or $FASnI_3$/$CsSnI_3$ (a). Efficiency and current density of $FASnI_3$/$CsSnI_3$ homojunction-based HTM-free PSC at maximum power point tracking (b), long-term stability of the $FASnI_3$-based devices and $FASnI_3$/$CsSnI_3$-based devices at 25 °C in air (c).

Author Contributions: Conceptualization, investigation, methodology, writing, review and editing, S.S.; Review and editing, formal analysis, supervision and validation, I.M.O.; Formal analysis, supervision and validation S.A.; Formal analysis, supervision and validation, I.B.S.; Conceptualization, methodology, review and editing J.P. All authors have read and agreed to the published version of the manuscript.

Institutional Review Board Statement: Not applicable.

Informed Consent Statement: Not applicable.

References

1. Čulík, P.; Brooks, K.; Momblona, C.; Adams, M.; Kinge, S.; Maréchal, F.; Dyson, P.J.; Nazeeruddin, M.K. Design and Cost Analysis of 100 MW Perovskite Solar Panel Manufacturing Process in Different Locations. *ACS Energy Lett.* **2022**, *7*, 3039–3044. [CrossRef]
2. Menda, U.D.; Ribeiro, G.; Nunes, D.; Calmeiro, T.; Águas, H.; Fortunato, E.; Martins, R.; Mendes, M.J. High-performance wide bandgap perovskite solar cells fabricated in ambient high-humidity conditions. *Mater. Adv.* **2021**, *2*, 6344–6355. [CrossRef]
3. Green, M.A.; Dunlop, E.D.; Hohl-Ebinger, J.; Yoshita, M.; Kopidakis, N.; Bothe, K.; Hinken, D.; Rauer, M.; Hao, X. Solar cell efficiency tables (Version 60). *Prog. Photovoltaics Res. Appl.* **2022**, *30*, 687–701. [CrossRef]
4. Sajid, S.; Elseman, A.M.; Huang, H.; Ji, J.; Dou, S.; Jiang, H.; Liu, X.; Wei, D.; Cui, P.; Li, M. Breakthroughs in NiOx-HTMs towards stable, low-cost and efficient perovskite solar cells. *Nano Energy* **2018**, *51*, 408–424. [CrossRef]
5. Elseman, A.M.; Sharmoukh, W.; Sajid, S.; Cui, P.; Ji, J.; Dou, S.; Wei, D.; Huang, H.; Xi, W.; Chu, L.; et al. Superior Stability and Efficiency Over 20% Perovskite Solar Cells Achieved by a Novel Molecularly Engineered Rutin–AgNPs/Thiophene Copolymer. *Adv. Sci.* **2018**, *5*, 1800568. [CrossRef]
6. Sajid, S.; Elseman, A.M.; Wei, D.; Ji, J.; Dou, S.; Huang, H.; Cui, P.; Li, M. NiO@carbon spheres: A promising composite electrode for scalable fabrication of planar perovskite solar cells at low cost. *Nano Energy* **2019**, *55*, 470–476. [CrossRef]
7. Elseman, A.M.; Sajid, S.; Shalan, A.E.; Mohamed, S.A.; Rashad, M.M. Recent progress concerning inorganic holetransport layers for efficient perovskite solar cells. *Appl. Phys. A* **2019**, *125*, 476. [CrossRef]
8. Sajid; Elseman, A.M.; Ji, J.; Dou, S.; Huang, H.; Cui, P.; Wei, D.; Li, M. Novel hole transport layer of nickel oxide composite with carbon for high-performance perovskite solar cells. *Chin. Phys. B* **2018**, *27*, 017305. [CrossRef]
9. Liang, J.; Hu, X.; Wang, C.; Liang, C.; Chen, C.; Xiao, M.; Li, J.; Tao, C.; Xing, G.; Yu, R.; et al. Origins and influences of metallic lead in perovskite solar cells. *Joule* **2022**, *6*, 816–833. [CrossRef]
10. Etgar, L.; Gao, P.; Xue, Z.; Peng, Q.; Chandiran, A.K.; Liu, B.; Nazeeruddin, M.K.; Grätzel, M. Mesoscopic $CH_3NH_3PbI_3/TiO_2$ heterojunction solar cells. *J. Am. Chem. Soc.* **2012**, *134*, 17396–17399. [CrossRef]
11. Mei, A.; Li, X.; Liu, L.; Ku, Z.; Liu, T.; Rong, Y.; Xu, M.; Hu, M.; Chen, J.; Yang, Y.; et al. A hole-conductor–free, fully printable mesoscopic perovskite solar cell with high stability. *Science* **2014**, *345*, 295–298. [CrossRef] [PubMed]
12. Chen, H.; Wei, Z.; He, H.; Zheng, X.; Wong, K.S.; Yang, S. Solvent Engineering Boosts the Efficiency of Paintable Carbon-Based Perovskite Solar Cells to Beyond 14%. *Adv. Energy Mater.* **2016**, *6*, 1502087. [CrossRef]
13. Wu, W.-Q.; Wang, Q.; Fang, Y.; Shao, Y.; Tang, S.; Deng, Y.; Lu, H.; Liu, Y.; Li, T.; Yang, Z. Molecular doping enabled scalable blading of efficient hole-transport-layer-free perovskite solar cells. *Nat. Commun.* **2018**, *9*, 1625. [CrossRef] [PubMed]
14. Kong, W.; Li, W.; Liu, C.; Liu, H.; Miao, J.; Wang, W.; Chen, S.; Hu, M.; Li, D.; Amini, A.; et al. Organic Monomolecular Layers Enable Energy-Level Matching for Efficient Hole Transporting Layer Free Inverted Perovskite Solar Cells. *ACS Nano* **2019**, *13*, 1625–1634. [CrossRef] [PubMed]
15. Ma, Z.; Yuan, S.; Deng, J.; Wang, M.; Wu, W.; Tian, D.; Lou, Z.; Li, W.; Fan, J. Small-Molecule Targeting of Defect Passivation in All-Inorganic Carbon-Based Perovskite Solar Cells. *Sol. RRL* **2023**, 2201079. [CrossRef]
16. Ke, W.; Kanatzidis, M.G. Prospects for low-toxicity lead-free perovskite solar cells. *Nat. Commun.* **2019**, *10*, 965. [CrossRef]
17. Nandy, S.; Fortunato, E.; Martins, R. Green economy and waste management: An inevitable plan for materials science. *Prog. Nat. Sci. Mater. Int.* **2022**, *32*, 1–9. [CrossRef]
18. Filippetti, A.; Kahmann, S.; Caddeo, C.; Mattoni, A.; Saba, M.; Bosin, A.; Loi, M.A. Fundamentals of tin iodide perovskites: A promising route to highly efficient, lead-free solar cells. *J. Mater. Chem. A* **2021**, *9*, 11812–11826. [CrossRef]
19. Lee, S.J.; Shin, S.S.; Kim, Y.C.; Kim, D.; Ahn, T.K.; Noh, J.H.; Seo, J.; Seok, S. Il Fabrication of efficient formamidinium tin iodide perovskite solar cells through SnF2–pyrazine complex. *J. Am. Chem. Soc.* **2016**, *138*, 3974–3977. [CrossRef]
20. Liao, W.; Zhao, D.; Yu, Y.; Grice, C.R.; Wang, C.; Cimaroli, A.J.; Schulz, P.; Meng, W.; Zhu, K.; Xiong, R. Lead-free inverted planar formamidinium tin triiodide perovskite solar cells achieving power conversion efficiencies up to 6.22%. *Adv. Mater.* **2016**, *28*, 9333–9340. [CrossRef]
21. Ke, W.; Stoumpos, C.C.; Zhu, M.; Mao, L.; Spanopoulos, I.; Liu, J.; Kontsevoi, O.Y.; Chen, M.; Sarma, D.; Zhang, Y. Enhanced photovoltaic performance and stability with a new type of hollow 3D perovskite {en} FASnI3. *Sci. Adv.* **2017**, *3*, e1701293. [CrossRef] [PubMed]
22. Zhu, Z.; Chueh, C.; Li, N.; Mao, C.; Jen, A.K. Realizing efficient lead-free formamidinium tin triiodide perovskite solar cells via a sequential deposition route. *Adv. Mater.* **2018**, *30*, 1703800. [CrossRef]
23. Liu, C.; Tu, J.; Hu, X.; Huang, Z.; Meng, X.; Yang, J.; Duan, X.; Tan, L.; Li, Z.; Chen, Y. Enhanced hole transportation for inverted tin-based perovskite solar cells with high performance and stability. *Adv. Funct. Mater.* **2019**, *29*, 1808059. [CrossRef]

24. Yang, Z.; Zhong, M.; Liang, Y.; Yang, L.; Liu, X.; Li, Q.; Zhang, J.; Xu, D. SnO2-C60 Pyrrolidine Tris-Acid (CPTA) as the Electron Transport Layer for Highly Efficient and Stable Planar Sn-Based Perovskite Solar Cells. *Adv. Funct. Mater.* **2019**, *29*, 1903621. [CrossRef]

25. Zhao, Z.; Gu, F.; Li, Y.; Sun, W.; Ye, S.; Rao, H.; Liu, Z.; Bian, Z.; Huang, C. Mixed-organic-cation tin iodide for lead-free perovskite solar cells with an efficiency of 8.12%. *Adv. Sci.* **2017**, *4*, 1700204. [CrossRef] [PubMed]

26. Liu, X.; Yan, K.; Tan, D.; Liang, X.; Zhang, H.; Huang, W. Solvent engineering improves efficiency of lead-free tin-based hybrid perovskite solar cells beyond 9%. *ACS Energy Lett.* **2018**, *3*, 2701–2707. [CrossRef]

27. Shao, S.; Liu, J.; Portale, G.; Fang, H.; Blake, G.R.; ten Brink, G.H.; Koster, L.J.A.; Loi, M.A. Highly reproducible Sn-based hybrid perovskite solar cells with 9% efficiency. *Adv. Energy Mater.* **2018**, *8*, 1702019. [CrossRef]

28. Wang, F.; Jiang, X.; Chen, H.; Shang, Y.; Liu, H.; Wei, J.; Zhou, W.; He, H.; Liu, W.; Ning, Z. 2D-quasi-2D-3D hierarchy structure for tin perovskite solar cells with enhanced efficiency and stability. *Joule* **2018**, *2*, 2732–2743. [CrossRef]

29. Jokar, E.; Chien, C.; Tsai, C.; Fathi, A.; Diau, E.W. Robust tin-based perovskite solar cells with hybrid organic cations to attain efficiency approaching 10%. *Adv. Mater.* **2019**, *31*, 1804835. [CrossRef]

30. Kamarudin, M.A.; Hirotani, D.; Wang, Z.; Hamada, K.; Nishimura, K.; Shen, Q.; Toyoda, T.; Iikubo, S.; Minemoto, T.; Yoshino, K. Suppression of charge carrier recombination in lead-free tin halide perovskite via Lewis base post-treatment. *J. Phys. Chem. Lett.* **2019**, *10*, 5277–5283. [CrossRef]

31. Jiang, X.; Li, H.; Zhou, Q.; Wei, Q.; Wei, M.; Jiang, L.; Wang, Z.; Peng, Z.; Wang, F.; Zang, Z. One-step synthesis of SnI2·(DMSO) x adducts for high-performance tin perovskite solar cells. *J. Am. Chem. Soc.* **2021**, *143*, 10970–10976. [CrossRef] [PubMed]

32. Tara, A.; Bharti, V.; Sharma, S.; Gupta, R. Device simulation of FASnI3 based perovskite solar cell with Zn(O0.3, S0.7) as electron transport layer using SCAPS-1D. *Opt. Mater.* **2021**, *119*, 111362. [CrossRef]

33. Bechtel, J.S.; Van der Ven, A. Octahedral tilting instabilities in inorganic halide perovskites. *Phys. Rev. Mater.* **2018**, *2*, 25401. [CrossRef]

34. Xiang, W.; Tress, W. Review on recent progress of all-inorganic metal halide perovskites and solar cells. *Adv. Mater.* **2019**, *31*, 1902851. [CrossRef]

35. Chen, L.-J.; Lee, C.-R.; Chuang, Y.-J.; Wu, Z.-H.; Chen, C. Synthesis and Optical Properties of Lead-Free Cesium Tin Halide Perovskite Quantum Rods with High-Performance Solar Cell Application. *J. Phys. Chem. Lett.* **2016**, *7*, 5028–5035. [CrossRef]

36. Song, T.-B.; Yokoyama, T.; Aramaki, S.; Kanatzidis, M.G. Performance Enhancement of Lead-Free Tin-Based Perovskite Solar Cells with Reducing Atmosphere-Assisted Dispersible Additive. *ACS Energy Lett.* **2017**, *2*, 897–903. [CrossRef]

37. Chung, I.; Song, J.-H.; Im, J.; Androulakis, J.; Malliakas, C.D.; Li, H.; Freeman, A.J.; Kenney, J.T.; Kanatzidis, M.G. CsSnI3: Semiconductor or metal? High electrical conductivity and strong near-infrared photoluminescence from a single material. High hole mobility and phase-transitions. *J. Am. Chem. Soc.* **2012**, *134*, 8579–8587. [CrossRef]

38. Sebastia-Luna, P.; Pokharel, U.; Huisman, B.A.H.; Koster, L.J.A.; Palazon, F.; Bolink, H.J. Vacuum-Deposited Cesium Tin Iodide Thin Films with Tunable Thermoelectric Properties. *ACS Appl. Energy Mater.* **2022**, *5*, 10216–10223. [CrossRef]

39. Gao, W.; Chen, C.; Ran, C.; Zheng, H.; Dong, H.; Xia, Y.; Chen, Y.; Huang, W. A-Site Cation Engineering of Metal Halide Perovskites: Version 3.0 of Efficient Tin-Based Lead-Free Perovskite Solar Cells. *Adv. Funct. Mater.* **2020**, *30*, 2000794. [CrossRef]

40. Yao, H.; Zhou, F.; Li, Z.; Ci, Z.; Ding, L.; Jin, Z. Strategies for Improving the Stability of Tin-Based Perovskite (ASnX3) Solar Cells. *Adv. Sci.* **2020**, *7*, 1903540. [CrossRef]

41. Lin, R.; Xiao, K.; Qin, Z.; Han, Q.; Zhang, C.; Wei, M.; Saidaminov, M.I.; Gao, Y.; Xu, J.; Xiao, M.; et al. Monolithic all-perovskite tandem solar cells with 24.8% efficiency exploiting comproportionation to suppress Sn(ii) oxidation in precursor ink. *Nat. Energy* **2019**, *4*, 864–873. [CrossRef]

42. Mahmoudi, T.; Rho, W.-Y.; Kohan, M.; Im, Y.H.; Mathur, S.; Hahn, Y.-B. Suppression of Sn2+/Sn4+ oxidation in tin-based perovskite solar cells with graphene-tin quantum dots composites in active layer. *Nano Energy* **2021**, *90*, 106495. [CrossRef]

43. Kumar, M.H.; Dharani, S.; Leong, W.L.; Boix, P.P.; Prabhakar, R.R.; Baikie, T.; Shi, C.; Ding, H.; Ramesh, R.; Asta, M.; et al. Lead-Free Halide Perovskite Solar Cells with High Photocurrents Realized through Vacancy Modulation. *Adv. Mater.* **2014**, *26*, 7122–7127. [CrossRef] [PubMed]

44. Kayesh, M.E.; Chowdhury, T.H.; Matsuishi, K.; Kaneko, R.; Kazaoui, S.; Lee, J.-J.; Noda, T.; Islam, A. Enhanced Photovoltaic Performance of FASnI3-Based Perovskite Solar Cells with Hydrazinium Chloride Coadditive. *ACS Energy Lett.* **2018**, *3*, 1584–1589. [CrossRef]

45. Marshall, K.P.; Walker, M.; Walton, R.I.; Hatton, R.A. Enhanced stability and efficiency in hole-transport-layer-free CsSnI3 perovskite photovoltaics. *Nat. Energy* **2016**, *1*, 16178. [CrossRef]

46. Li, W.; Li, J.; Li, J.; Fan, J.; Mai, Y.; Wang, L. Addictive-assisted construction of all-inorganic CsSnIBr 2 mesoscopic perovskite solar cells with superior thermal stability up to 473 K. *J. Mater. Chem. A* **2016**, *4*, 17104–17110. [CrossRef]

47. Song, T.-B.; Yokoyama, T.; Stoumpos, C.C.; Logsdon, J.; Cao, D.H.; Wasielewski, M.R.; Aramaki, S.; Kanatzidis, M.G. Importance of Reducing Vapor Atmosphere in the Fabrication of Tin-Based Perovskite Solar Cells. *J. Am. Chem. Soc.* **2017**, *139*, 836–842. [CrossRef]

48. Ke, W.; Stoumpos, C.C.; Spanopoulos, I.; Mao, L.; Chen, M.; Wasielewski, M.R.; Kanatzidis, M.G. Efficient Lead-Free Solar Cells Based on Hollow {en}MASnI3 Perovskites. *J. Am. Chem. Soc.* **2017**, *139*, 14800–14806. [CrossRef]

49. Nakamura, T.; Yakumaru, S.; Truong, M.A.; Kim, K.; Liu, J.; Hu, S.; Otsuka, K.; Hashimoto, R.; Murdey, R.; Sasamori, T. Sn (IV)-free tin perovskite films realized by in situ Sn (0) nanoparticle treatment of the precursor solution. *Nat. Commun.* **2020**, *11*, 3008. [CrossRef]

50. Kim, J.; Lee, S.-H.; Lee, J.H.; Hong, K.-H. The role of intrinsic defects in methylammonium lead iodide perovskite. *J. Phys. Chem. Lett.* **2014**, *5*, 1312–1317. [CrossRef]

51. Wang, Q.; Shao, Y.; Xie, H.; Lyu, L.; Liu, X.; Gao, Y.; Huang, J. Qualifying composition dependent p and n self-doping in CH3NH3PbI3. *Appl. Phys. Lett.* **2014**, *105*, 163508. [CrossRef]

52. Frolova, L.A.; Dremova, N.N.; Troshin, P.A. The chemical origin of the p-type and n-type doping effects in the hybrid methylammonium–lead iodide (MAPbI 3) perovskite solar cells. *Chem. Commun.* **2015**, *51*, 14917–14920. [CrossRef] [PubMed]

53. Danekamp, B.; Müller, C.; Sendner, M.; Boix, P.P.; Sessolo, M.; Lovrincic, R.; Bolink, H.J. Perovskite–perovskite homojunctions via compositional doping. *J. Phys. Chem. Lett.* **2018**, *9*, 2770–2775. [CrossRef] [PubMed]

54. Ran, C.; Xu, J.; Gao, W.; Huang, C.; Dou, S. Defects in metal triiodide perovskite materials towards high-performance solar cells: Origin, impact, characterization, and engineering. *Chem. Soc. Rev.* **2018**, *47*, 4581–4610. [CrossRef]

55. Cui, P.; Wei, D.; Ji, J.; Huang, H.; Jia, E.; Dou, S.; Wang, T.; Wang, W.; Li, M. Planar p–n homojunction perovskite solar cells with efficiency exceeding 21.3%. *Nat. Energy* **2019**, *4*, 150–159. [CrossRef]

56. Chowdhury, M.S.; Rahman, K.S.; Selvanathan, V.; Hasan, A.K.M.; Jamal, M.S.; Samsudin, N.A.; Akhtaruzzaman, M.; Amin, N.; Techato, K. Recovery of FTO coated glass substrate via environment-friendly facile recycling perovskite solar cells. *RSC Adv.* **2021**, *11*, 14534–14541. [CrossRef] [PubMed]

57. Bisht, H.; Eun, H.-T.; Mehrtens, A.; Aegerter, M.A. Comparison of spray pyrolyzed FTO, ATO and ITO coatings for flat and bent glass substrates. *Thin Solid Films* **1999**, *351*, 109–114. [CrossRef]

58. Wojciechowski, K.; Saliba, M.; Leijtens, T.; Abate, A.; Snaith, H.J. Sub-150 °C processed meso-superstructured perovskite solar cells with enhanced efficiency. *Energy Environ. Sci.* **2014**, *7*, 1142–1147. [CrossRef]

59. O'Regan, B.C.; Durrant, J.R.; Sommeling, P.M.; Bakker, N.J. Influence of the TiCl4 treatment on nanocrystalline TiO2 films in dye-sensitized solar cells. 2. Charge density, band edge shifts, and quantification of recombination losses at short circuit. *J. Phys. Chem. C* **2007**, *111*, 14001–14010. [CrossRef]

60. Milot, R.L.; Eperon, G.E.; Green, T.; Snaith, H.J.; Johnston, M.B.; Herz, L.M. Radiative monomolecular recombination boosts amplified spontaneous emission in HC (NH2) 2SnI3 perovskite films. *J. Phys. Chem. Lett.* **2016**, *7*, 4178–4184. [CrossRef]

61. Dang, Y.; Zhou, Y.; Liu, X.; Ju, D.; Xia, S.; Xia, H.; Tao, X. Formation of hybrid perovskite tin iodide single crystals by top-seeded solution growth. *Angew. Chemie Int. Ed.* **2016**, *55*, 3447–3450. [CrossRef]

62. Stoumpos, C.C.; Malliakas, C.D.; Kanatzidis, M.G. Semiconducting tin and lead iodide perovskites with organic cations: Phase transitions, high mobilities, and near-infrared photoluminescent properties. *Inorg. Chem.* **2013**, *52*, 9019–9038. [CrossRef]

63. Khan, D.; Sajid, S.; Khan, S.; Park, J.; Ullah, I. Identifying the potentials for charge transport layers free n-p homojunction-based perovskite solar cells. *Sol. Energy* **2022**, *238*, 69–77. [CrossRef]

64. Sajid, S.; Mourtada, A.; Jun, E.; Shangyi, J.; Dong, D.; Hao, W.; Peng, H. Computational Study of Ternary Devices: Stable, Low-Cost, and Efficient Planar Perovskite Solar Cells. *Nano-Micro Lett.* **2018**, *10*, 51. [CrossRef]

65. Sajid, S.; Alzahmi, S.; Salem, I.B.; Obaidat, I.M. Guidelines for Fabricating Highly Efficient Perovskite Solar Cells with Cu2O as the Hole Transport Material. *Nanomaterials* **2022**, *12*, 3315. [CrossRef]

66. Ming, W.; Yang, D.; Li, T.; Zhang, L.; Du, M. Formation and diffusion of metal impurities in perovskite solar cell material CH3NH3PbI3: Implications on solar cell degradation and choice of electrode. *Adv. Sci.* **2018**, *5*, 1700662. [CrossRef]

67. Pydzińska-Białek, K.; Nowaczyk, G.; Ziółek, M. Complete Perovskite Solar Cells with Gold Electrodes Studied in the Visible and Near-Infrared Ranges. *Chem. Mater.* **2022**, *34*, 6355–6366. [CrossRef]

68. Burgelman, M.; Nollet, P.; Degrave, S. Modelling polycrystalline semiconductor solar cells. *Thin Solid Films* **2000**, *361–362*, 527–532. [CrossRef]

69. Wang, T.; Chen, J.; Wu, G.; Li, M. Optimal design of efficient hole transporting layer free planar perovskite solar cell. *Sci. China Mater.* **2016**, *59*, 703–709. [CrossRef]

70. Wang, N.; Zhou, Y.; Ju, M.-G.; Garces, H.F.; Ding, T.; Pang, S.; Zeng, X.C.; Padture, N.P.; Sun, X.W. Heterojunction-Depleted Lead-Free Perovskite Solar Cells with Coarse-Grained B-γ-CsSnI3 Thin Films. *Adv. Energy Mater.* **2016**, *6*, 1601130. [CrossRef]

71. Buin, A.; Pietsch, P.; Xu, J.; Voznyy, O.; Ip, A.H.; Comin, R.; Sargent, E.H. Materials processing routes to trap-free halide perovskites. *Nano Lett.* **2014**, *14*, 6281–6286. [CrossRef] [PubMed]

72. Yu, H.; Wang, F.; Xie, F.; Li, W.; Chen, J.; Zhao, N. The role of chlorine in the formation process of "CH3NH3PbI3-xClx" perovskite. *Adv. Funct. Mater.* **2014**, *24*, 7102–7108. [CrossRef]

73. Chen, M.; Ju, M.-G.; Garces, H.F.; Carl, A.D.; Ono, L.K.; Hawash, Z.; Zhang, Y.; Shen, T.; Qi, Y.; Grimm, R.L. Highly stable and efficient all-inorganic lead-free perovskite solar cells with native-oxide passivation. *Nat. Commun.* **2019**, *10*, 16. [CrossRef] [PubMed]

74. Alexander, A.; Srivastava, V.; Ravichandran, P.; Pulikodan, V.K.; Anitha, B.; Joseph, A.; Namboothiry, M.A.G. Acetylammonium chloride as an additive for crystallization control and defect passivation in MAPbI3 based perovskite solar cells. *J. Phys. D. Appl. Phys.* **2022**, *55*, 265501. [CrossRef]

75. Devi, N.; Parrey, K.A.; Aziz, A.; Datta, S. Numerical simulations of perovskite thin-film solar cells using a CdS hole blocking layer. *J. Vac. Sci. Technol. B Nanotechnol. Microelectron. Mater. Process. Meas. Phenom.* **2018**, *36*, 04G105. [CrossRef]

76. Mesquita, I.; Andrade, L.; Mendes, A. Temperature Impact on Perovskite Solar Cells Under Operation. *ChemSusChem* **2019**, *12*, 2186–2194. [CrossRef]

77. Hao, F.; Stoumpos, C.C.; Guo, P.; Zhou, N.; Marks, T.J.; Chang, R.P.H.; Kanatzidis, M.G. Solvent-mediated crystallization of CH3NH3SnI3 films for heterojunction depleted perovskite solar cells. *J. Am. Chem. Soc.* **2015**, *137*, 11445–11452. [CrossRef]

78. Yokoyama, T.; Cao, D.H.; Stoumpos, C.C.; Song, T.-B.; Sato, Y.; Aramaki, S.; Kanatzidis, M.G. Overcoming Short-Circuit in Lead-Free CH3NH3SnI3 Perovskite Solar Cells via Kinetically Controlled Gas–Solid Reaction Film Fabrication Process. *J. Phys. Chem. Lett.* **2016**, *7*, 776–782. [CrossRef]

79. Gupta, S.; Bendikov, T.; Hodes, G.; Cahen, D. CsSnBr3, a lead-free halide perovskite for long-term solar cell application: Insights on SnF2 addition. *ACS Energy Lett.* **2016**, *1*, 1028–1033. [CrossRef]

80. Liu, X.; Wang, Y.; Xie, F.; Yang, X.; Han, L. Improving the performance of inverted formamidinium tin iodide perovskite solar cells by reducing the energy-level mismatch. *ACS Energy Lett.* **2018**, *3*, 1116–1121. [CrossRef]

81. Akbulatov, A.F.; Tsarev, S.A.; Elshobaki, M.; Luchkin, S.Y.; Zhidkov, I.S.; Kurmaev, E.Z.; Aldoshin, S.M.; Stevenson, K.J.; Troshin, P.A. Comparative Intrinsic Thermal and Photochemical Stability of Sn(II) Complex Halides as Next-Generation Materials for Lead-Free Perovskite Solar Cells. *J. Phys. Chem. C* **2019**, *123*, 26862–26869. [CrossRef]

82. Ye, T.; Wang, K.; Hou, Y.; Yang, D.; Smith, N.; Magill, B.; Yoon, J.; Mudiyanselage, R.R.H.H.; Khodaparast, G.A.; Wang, K.; et al. Ambient-Air-Stable Lead-Free CsSnI3 Solar Cells with Greater than 7.5% Efficiency. *J. Am. Chem. Soc.* **2021**, *143*, 4319–4328. [CrossRef] [PubMed]

83. Meng, X.; Wang, Y.; Lin, J.; Liu, X.; He, X.; Barbaud, J.; Wu, T.; Noda, T.; Yang, X.; Han, L. Surface-Controlled Oriented Growth of FASnI3 Crystals for Efficient Lead-free Perovskite Solar Cells. *Joule* **2020**, *4*, 902–912. [CrossRef]

84. Lin, C.; Hu, L.; Guan, X.; Kim, J.; Huang, C.; Huang, J.; Singh, S.; Wu, T. Electrode engineering in halide perovskite electronics: Plenty of room at the interfaces. *Adv. Mater.* **2022**, *34*, 2108616. [CrossRef]

85. Laska, M.; Krzemińska, Z.; Kluczyk-Korch, K.; Schaadt, D.; Popko, E.; Jacak, W.A.; Jacak, J.E. Metallization of solar cells, exciton channel of plasmon photovoltaic effect in perovskite cells. *Nano Energy* **2020**, *75*, 104751. [CrossRef]

86. Jacak, J.E.; Jacak, W.A. Routes for Metallization of Perovskite Solar Cells. *Materials* **2022**, *15*, 2254. [CrossRef]